Variations in probability distributions as indicators of seismic phases: a case study from Chile

R. Rotondi[1], O. Nicolis[2,3], E. Varini[*1], and F. Ruggeri[1]

Abstract

In this study, we analyze the seismic activity of Chile, a region known for its diverse seismic characteristics, to validate and strengthen our findings on the identification of indicators of precursory phases. We employ Bayesian inference, processing data through sliding time windows. Each window contains a fixed number of events and shifts with each new event. Regarding the temporal variations in magnitude distribution, we observe similar patterns in seismic sequences in both Italy and Chile. The estimated q-index significantly decreases before strong earthquakes and increases sharply afterward, indicating its potential as a marker of the activation state of these systems. Additionally, in analyzing the spatial distances between successive earthquakes we consider various distributions, such as tapered Pareto and generalized gamma. The optimal distribution for each time window is selected by comparing the estimated values of the posterior marginal likelihood. We discover that the best-fitting distribution changes over time, serving as an additional indicator of the activation state of the systems.

Cite this article as Rotondi R., O. Nicolis, E. Varini and F. Ruggeri (2022). Variations in probability distributions as indicators of seismic phases: a case study from Chile, *Seismol. Res. Lett.* **XX**, 1–15, doi: 00.0000/000000000.

Supplemental Material

Introduction

The seismicity along the coast of Chile is among the highest in the world, primarily due to the subduction of the Nazca Plate beneath the South American Plate, which causes the moving eastward of the Nazca Plate with an average velocity rate of about 70-80 mm per year. This process generates significant seismic activity, including frequent and often powerful earthquakes (Barrientos and Team, 2018). The seismicity in this area is also influenced by the Iquique ridge, a prominent bathymetric feature on the Nazca Plate, off the coast of northern Chile. This plays a significant role in the region's tectonic activity by influencing the subduction dynamics: the ridge's interaction with the subduction zone leads to variations in stress accumulation and seismic activity, contributing to the seismic hazards in northern Chile (Contreras-Reyes et al., 2021). The 2014 Iquique earthquake, which occurred on 1 April 2014 with magnitude 8.2, is a significant event that highlights the seismic characteristics of this area (Hayes et al., 2014; Ma et al., 2023). Meng et al. (2015) discuss different slip behaviors on the megathrust, particularly near the Iquique Ridge, highlighting how these behaviors influenced overall seismic activity and specifically impacted the ridge area. It is also important to note that this large earthquake is preceded by an unusual series of foreshocks and a slow slip event, as revealed by the GPS data analysis (Ruiz et al., 2014). These precursory activities provide crucial insights into the mechanisms that lead to large earthquakes. Schurr et al. (2014) emphasize the role of foreshock activity and seismic coupling in the gradual unlocking of the plate boundary, leading to the mainshock. Hayes et al. (2014) examine the implications of the 2014 Iquique event for future seismic hazards, noting that only a portion of the seismic gap was ruptured, leaving significant segments still locked and posing a threat for potentially more powerful future earthquakes. These studies collectively enhance our understanding of seismic behavior in northern Chile, emphasizing the ongoing risks and the complex interplay of geological forces in this tectonically active region. In this study we statistically analyze the sequence of earthquakes occurred in northern Chile from January 2011 to January 2024, which includes the Iquique earthquake.

Recently some studies have been conducted in the field of non-extensive statistical mechanics (NESM) for understanding the complex dynamic system of seismic phenom-

1. National Research Council of Italy, Institute for Applied Mathematics and Information Technologies Enrico Magenes, Milano, Italy, https://orcid.org/0000-0003-1501-9751 (RR) https://orcid.org/0000-0002-5365-4249 (EV) https://orcid.org/0000-0002-7655-6254 (FR); 2. Universidad Andres Bello, Engineering Faculty, Viña del Mar, Chile, https://orcid.org/0000-0001-8046-6983 (ON); 3. Research Center for Integrated Disaster Risk Management (CIGIDEN), Santiago, Region Metropolitana, Chile, https://orcid.org/0000-0001-8046-6983 (ON)

*Corresponding author: elisa.varini@cnr.it

ena which traditional methods might not fully capture. In this context, Posadas and Sotolongo-Costa (2023) develop a fragment-asperity interaction model which explains the physical process of earthquake generation; they also propose the q-exponential probability distribution derived from the Tsallis entropy as distribution for the surface of the fragments and, through a transformation of variables, they obtain a new probability distribution for the magnitude that is characterized by the so-called q entropic index.

Successively, Posadas et al. (2023) verify that the Shannon entropy can serve as an indicator of the equilibrium state of a seismically active region in which increasing entropy is linked to the occurrence of large earthquakes; the case of northern Chile is considered as an application. NESM is also explored by Vallianatos et al. (2016) as a consistent statistical framework for describing seismicity and faulting, highlighting its applicability across different tectonic environments. The approach is seen as beneficial in modeling earthquakes as 'phase transitions' in the statistical mechanical view, integrating the physics of earthquakes into a more comprehensive theoretical framework.

Rotondi et al. (2022) use the q-exponential distribution to investigate the time evolution of the seismic activity in Central Italy; in particular, they show how the q entropic index and Tsallis entropy, evaluated over a fixed number of the magnitude data contained in shifting time windows, have different patterns before and after significant earthquakes so that they can be used as indicators for earthquake prediction. In Rotondi and Varini (2022) the spatial distribution of seismic events is examined by comparing various probability distributions for the area of the cells of the Voronoi tessellation generated by their epicenters; also in this case changes in the best model can be associated with different phases in the seismic cycle. An analogous approach is used in Varini and Rotondi (2023) to find temporal variations in the probability distribution of the recurrence time separating two consecutive earthquakes.

Following this research line, in this work we analyze the seismicity of northern Chile to verify whether there is some connection between variations of the probability model of some seismic quantities and changes in seismic phases.

The data set

The dataset used in this study was provided by the National Seismological Center of the University of Chile (http://www.csn.uchile.cl). It includes latitude and longitude (in decimal degrees), depth (in kilometers), magnitude, and date and time of occurrence for seismic events in Chile from 2003 to January 2024. Although the Chilean catalogue is available from 2000, Chile significantly developed and enhanced its seismic network after the devastating 2010 Maule earthquake (see Barrientos and Team, 2018), ensuring comprehensive coverage across almost all areas of the country. Therefore, this is a first indication for considering the historical events starting from 2011.

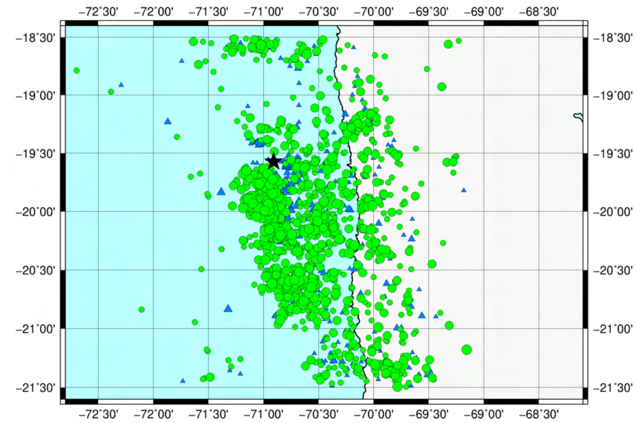

Figure 1: Earthquakes of $M \geq 3.4$ before (triangles) and after (circles) the Iquique mainshock on 1 April 2014. The star denotes the epicenter.

From the Chilean catalogue covering the period from 2003 to January 2024, we extract $N = 7302$ events of magnitude $1.5 \leq M \leq 8.2$ and depth less than 70 kms, which belong to the rectangular area of latitude size (-21.5; -18.5) degrees and longitude size (-72.7; -68.2) degrees; these data include the strong earthquake occurred on April 1, 2014 of magnitude 8.2. A graphical exploratory analysis of the data set, reported in *Supplemental Material*, shows that the set can be considered sufficiently complete with magnitude threshold $m_0 = 3.4$ since 2011. However, we are aware that a partial incompleteness remains in the hours immediately following the main shock, but we think that it does not bias significantly the results as observed in previous studies (Rotondi et al., 2022); it is caused both by the duration of the main shock and by a high number of smaller magnitude events whose waveforms overlap. We consider the data set represented in Figure 1, consisting of $N = 2143$ events with $M \geq 3.4$ recorded from January 2011 to January 2024.

In Table 1 we report the events of magnitude larger than or equal to 6 recorded since 2011.

Theoretical elements

The basic theoretical elements involved in our analysis are briefly summarized below, mainly referring to Rotondi et al. (2022) and Rotondi and Varini (2022) for further details.

Probability model for the magnitude

According to the Gutenberg-Richter empirical law, the earthquake magnitude follows the exponential distribution, whose probability density function (pdf) is given in (1), for $\lambda > 0$.

$$f_1(x) = \lambda\, e^{-\lambda\, x}\,, \quad x > 0 \tag{1}$$

TABLE 1. : The date and occurrence time of the earthquakes with $M \geq 6.0$ included in the northern Chile sequence under consideration (UTC time). The magnitudes $M \geq 7$ are in boldface.

Year	Month	Day	Hour	Minute	Second	M
2014	3	16	21	16	29	6.7
2014	3	17	5	11	34	6.3
2014	3	23	18	20	0	6.1
2014	4	1	23	46	45	**8.2**
2014	4	1	23	49	25	**7.5**
2014	4	1	23	52	18	6.6
2014	4	1	23	57	59	**7.0**
2014	4	1	23	58	5	6.6
2014	4	3	1	58	31	6.3
2014	4	3	2	43	15	**7.6**
2014	4	3	5	26	15	6.3
2014	4	4	1	37	52	6.1
2014	4	7	13	43	20	6.1
2014	4	11	0	1	44	6.2
2014	6	19	19	54	5	6.0
2019	12	3	8	46	34	6.0
2020	9	11	7	35	56	6.0

In NESM, the q-exponential distribution is used to represent physical quantities that characterize a complex system, such as the earthquake generation process. Its pdf arises from the maximization of the Tsallis entropy under suitable constraints; this entropy is non-additive, that is, the total entropy of two separate systems is smaller (subadditive state) or greater (superadditive state) than the sum of the entropies of each system. As a consequence, the q-exponential pdf has two different expressions depending on the value of the entropic index q, one for the subadditive state for $1 < q < 2$ and one for the superadditive state for $q < 1$. Only the former $(1 < q < 2)$ is used in this work and shown below:

$$f_2(x) = \frac{1}{\eta}\left(1 - \frac{(1-q)}{(2-q)}\,\frac{x}{\eta}\right)^{1/(1-q)} \qquad 1 < q < 2\,, \quad x > 0 \tag{2}$$

Indeed, the pdf for $q < 1$ has an upside down shape, which was found to fit data with many missing low magnitude events, such as the aftershock sequences in the early period following the mainshock; these circumstances proved to be of negligible importance for the purposes of this study (more details in Rotondi et al., 2022).

In the subadditive case $(1 < q < 2)$, the q-exponential distribution has tails with power law behavior, heavier than the exponential tails, indicating that large magnitude values are more likely in the former distribution than in the latter. It is also worth noting that if q approaches 1, then the exponential distribution is achieved.

In the application to the study of earthquake magnitude distribution, both exponential (1) and q-exponential (2) models are truncated on the support $[m_0, \infty)$, where m_0 is the minimum magnitude threshold which guarantees the earthquake catalogue completeness. Moreover, if x in (1) represents the earthquake magnitude M, then the exponential distribution in (3) is obtained, which corresponds to the well-known Gutenberg-Richter empirical law. Instead, the probability distribution of magnitude in (4) is obtained from the fragment-asperity interaction model, formulated by Sotolongo-Costa and Posadas (2004) in the frame of NESM. This model assumes that the surface x of fragments between the fault planes is q-exponentially distributed. Through empirical relationships, the size of the fragments is then related to the magnitude according to the relation $x \propto 10^M$ (x proportional to 10^M) which, substituted in (2) and after limiting the support to $M \in (m_0, \infty)$, provides (4) :

$$\frac{f_1(M)}{1 - F_1(m_0)} = \lambda\, e^{-\lambda\,(M - m_0)} \tag{3}$$

$$\frac{f_2(M)}{1 - F_2(m_0)} = \frac{(\ln 10)\,\dfrac{10^M}{\eta'}\left[1 + \dfrac{10^M}{\rho\eta'}\right]^{-(1+\rho)}}{\left[1 + \dfrac{10^{m_0}}{\rho\eta'}\right]^{-\rho}} \tag{4}$$

where $\eta' > 0$ and $\rho > 0$. Due to the non linear change of variable from x to M, the model (4) of the magnitude is not a q-exponential distribution but is derived from it; for simplicity, we will still use the term q-exponential for the model (4) hereafter. In particular, there is a one-to-one relation between ρ and the entropic index $q \in (1, 2)$ such that $q = (2 + \rho)/(1 + \rho)$.

Probability models for the area of Voronoi cells

The Voronoi diagram provides a partition of a region into convex polygons (cells) defined by a set P of n points (seeds) in the region. Each polygon contains exactly one seed and every point in a given polygon is closer to its seed than to any other. If one joins the seeds associated with any pair of cells that have an edge in common, we obtain a complete coverage of the convex hull of P made by non-overlapping triangles called Delaunay triangulation.

In our application the seeds are the epicenters of the earthquakes on the basis of which the seismic region under study is then divided into Voronoi cells (Rotondi and Varini, 2022). The aim is to investigate the spatial properties of the seismicity by analyzing the probability distribution of the area of the Voronoi cells, intended as a measure of spatial distances between earthquakes. We propose four different probability distribution functions to model the area of the Voronoi cells: the exponential, the q-exponential, the tapered Pareto and the generalized gamma distributions.

The first is considered as a basic probability model for data with decreasing trend as well as a limiting case of the q-exponential distribution for q approaching 1. For its part, the q-exponential arises in the framework of the nonextensive statistical physics by applying the principle of maximum entropy under appropriate constraints to the Tsallis entropy (Tsallis, 2009) and in statistical seismology it is applied to the surface of the fragments in the fragment-asperity interaction model for the earthquake generation by Sotolongo-Costa and Posadas (2004) ; by analogy we adopt this probability distribution for the surface of the Voronoi cells. The other two distributions were proposed in the literature to study the statistical characteristics of spatial point patterns from the geometrical characteristics of the corresponding tessellation; in particular Gezer et al. (2021) took into consideration the area of cells in the infinite plane and of cropped cells in bounded regions and found that the generalized gamma provided a good fit to different data sets, while Schoenberg et al. (2009) extended the application of the tapered Pareto distribution, adopted by Jackson and Kagan (1999) to describe the seismic moment, to the Voronoi tessellation.

The probability density functions of the exponential and q-exponential models are given in (1) and (2) respectively; those of the tapered Pareto and the generalized gamma models are as follows:

$$f_3(x) = \left(\frac{\beta}{x} + \frac{1}{\alpha}\right) \left(\frac{c}{x}\right)^{\beta} \exp\left(-\frac{x-c}{\alpha}\right) \quad x \geq c \tag{5}$$

$$f_4(x) = \frac{1}{\sigma\, x} \cdot \frac{\gamma\, (\gamma^{-2})^{\gamma^{-2}}}{\Gamma(\gamma^{-2})} \cdot \exp\left\{ \frac{\gamma\left(\frac{\ln x - \mu}{\sigma}\right) - \exp\left\{\gamma\left(\frac{\ln x - \mu}{\sigma}\right)\right\}}{\gamma^2} \right\} \tag{6}$$

In (5), the parameter $c > 0$ is the minimum of x, $\alpha > 0$ controls the position of the upper extreme of the linear portion of the log–log plot of the survival function, and $\beta > 0$ is a shape parameter controlling the power-law behavior (Vere-Jones et al., 2001). The generalized gamma distribution proposed by Prentice (1974) is shown in (6), which is a reparametrization of the original formulation by Stacy (1962). The shape and scale parameters are both positive and denoted by γ and σ, respectively, while the location parameter μ ranges on the real line. This reparametrization simplifies and greatly improves computational efficiency. Further details are given in Rotondi and Varini (2022).

Bayesian inference

Let us assume that the data $\boldsymbol{x} = (x_1, x_2, \dots, x_N)$ are realizations of a random variable $\mathcal{X}$ whose density function belongs to the parametric family $\mathcal{F} = \{f(x;\theta) \,:\, \theta \in \Theta\}$. According to the Bayesian paradigm, the parameter θ is considered as a random variable and its *prior* density function $p_0(\theta)$ expresses the initial beliefs on the phenomenon under examination. Bayes' theorem therefore allows the *prior* information to be combined with that provided by the data and expressed by the likelihood $\mathcal{L}(f(\boldsymbol{x} \mid \theta)) = \prod_{i=1}^{N} f(x_i;\theta)$ so as to obtain the *posterior* density distribution:

$$p(\theta \mid \boldsymbol{x}) = \frac{p_0(\theta)\, \mathcal{L}(f(\boldsymbol{x} \mid \theta))}{\int_\Theta p_0(\theta)\, \mathcal{L}(f(\boldsymbol{x} \mid \theta))\, d\theta} \quad . \tag{7}$$

The *posterior* distribution of θ provides the parameter estimate, typically as the posterior mean $\hat{\theta} = E_p(\theta)$, as well as statistical measures of the uncertainty such as, for example, posterior variance or quartiles. The plug-in distribution $f(\boldsymbol{x} \mid \hat{\theta})$, to be considered later, is obtained replacing the parameters in the model with their posterior means.

For the exponential model (1) the conjugate prior gamma distribution gives a closed-form expression for the posterior distribution (7) of the parameter λ; we therefore adopt as prior the Gamma(2.3,1) in the magnitude case, being $E_0(\lambda) = b\, \log 10 = 2.3$ because the parameter b of the Gutenberg-Richter law is approximately 1, and Gamma(10^{-3},1) in the cell area case being $E_0(\lambda) = 10^{-3}$ the inverse of the average cell area (in km^2). For the other models, due to the computational issues in evaluating the integral in (7), which is often multidimensional, we applied the Markov chain Monte Carlo method of Metropolis–Hastings (MH) to generate a sequence of random samples that closely approximates the posterior distribution (Robert and Casella, 2004). Starting from an initial parameter value θ_0 drawn from its prior density $p_0(\theta)$, the Metropolis–Hastings algorithm iteratively generates the Markov chain $\{\theta_0, \theta_1, \dots, \theta_S\}$ through an acceptance-rejection mechanism of sample values from an arbitrary probability density $q(\theta \mid \theta_i)$, called *proposal* density.

As prior distribution of each parameter θ we adopt a Lognormal($mean_\theta$, var_θ) distribution, where $mean_\theta$ and var_θ indicate the mean and variance of the random variable and not the mean and variance of its logarithm, as in the common representation of the lognormal distribution. We also choose lognormal distributions as proposal distributions; in particular, at the $(i+1)$-th iteration, we have Lognormal $(\theta_i, (\theta_i/\kappa)^2)$ where θ_i is the current value of the respective Markov chain and the value of κ is initially calibrated through pilot runs on the data so that the acceptance rate of the MH algorithm is about 25% to 40%; during the program this rate is maintained by automatically updating the value of κ. Table 2 reports the hyperparameters of the Lognormal prior distributions and the κ coefficient for the parameters of each model.

In the MH algorithm, to reduce the dependence on the initial sample θ_0 and also the correlation within the generated Markov chain, we neglect the first 10, 000 samples and then

TABLE 2. : Hyperparameters of the prior distributions and κ coefficients used in the proposal distributions in the MH algorithm.

Magnitude model	**parameters**	**mean$_0$**	**var$_0$**	κ
q-exponential	θ	0.5	0.25	2.8
	η'	25	64	0.8
Voronoi cell area model	**parameters**	**mean$_0$**	**var$_0$**	κ
q-exponential	θ	2	0.1	2.2
	η	7.5×10^2	55×10^4	1.9
tapered Pareto	α	20	100	2.6
	c	1.5	2.25	0.8
	β	0.1	0.01	0.7
generalized gamma	μ	7	50	12
	σ	2	1	4
	γ	0.3	0.1	0.4

we save a sample every 50 iterations to finally get a Markov chain of length $S = 9,800$.

Model comparison

Let $\mathcal{L}_{log}(f(\mathbf{x})) = \int_\Theta \log \mathcal{L}(f(\mathbf{x} \mid \theta))\, p(\theta \mid \mathbf{x})\, d\theta$ indicate the log-likelihood marginalized with respect to the posterior distribution $p(\theta \mid \mathbf{x})$ of the parameter θ; by the integration with respect the posterior distribution, we take into account the uncertainty in the parameter estimation. We can compare two distributions f_1 and f_2 through the discrepancy $\Delta_{1,2} = \mathcal{L}_{log}(f_1(\mathbf{x})) - \mathcal{L}_{log}(f_2(\mathbf{x}))$ between their marginal log-likelihoods and, as is done with the Bayes factor, we establish the level of evidence in favor of the first model according to the value $\mathcal{K}$ of the Jeffreys scale (Kass and Raftery, 1995; Gelman et al., 2004). In particular for each k-th time window we denote as best model the probability function f_{i^*} such that $i^* = \arg\max_{i=1,\dots,4} \mathcal{L}_{log}(f_i(\mathbf{x}^{(\mathbf{k})}))$ and the strength of the evidence in favor of this model is strong if $\Delta^{(k)}_{i^*,j} \geq \log_e 10 = 2.3026$ with $j = 1, \dots, 4$, and $j \neq i^*$, while it is worth no more than a bare mention if $0 < \Delta^{(k)}_{i^*,j} < 1.1513$.

The use of the posterior marginal log-likelihood as a tool to compare two models $M_1 = \{f_1(\mathbf{x}|\theta_1), p_1(\theta_1)\}$ and $M_2 = \{f_2(\mathbf{x}|\theta_2), p_2(\theta_2)\}$, where p_1 and p_2 are prior distributions, can be interpreted in a Bayesian decision theoretic framework: if we consider the negative log-likelihood as a loss function depending on the model M_i and the parameter θ_i, $i = 1, 2$, then the posterior marginal log-likelihood becomes the opposite of the posterior expected loss when choosing the model M_i. Following the subjective expected loss principle, we look for the model which minimizes the posterior expected loss, that is, maximizes the posterior marginal log-likelihood.

Analysis of the magnitude

We ask ourselves whether the distribution of the magnitudes varies over time and whether the different phases of the seismic cycle can be identified by variations in this distribution. To investigate this topic we take into account time windows of 100 events that move with each new event within the seismic sequence and, by following the Bayesian paradigm, we estimate the probability distribution of the magnitude on each data set thus obtained. We choose to examine 100 events in each window to balance two requirements: the accuracy of the parameter estimates and the detail of the analysis; the same value (100) has already been used in several works in literature (Lasocki et al., 2024). We performed a sensitivity analysis varying the number of events between 50 and 200; the results, reported in detail in the Supplemental Material, show that the conclusions remain substantially the same.

Since the Earth's crust is a complex, nonlinear dynamic system characterized by long-range correlations we address the problem in the framework of nonextensive statistical physics (Tsallis, 1988), adopting the probability distribution of magnitude in (4) derived from the q-exponential distribution with $q \in (1, 2)$ (Vallianatos et al., 2016), that has a heavy tail with power law behavior. For details on this distribution and on the Bayesian estimation method we refer to the previous section *Theoretical elements*.

Figure 2 shows the value of the q index estimated in each time window by associating it with the time of the last event present in the window itself (i.e. the occurrence time of the hundredth event in that window). Although the panels in Figure 2 include the same number (128) of q estimates, they cover quite different time intervals, as indicated above them; this also highlights variations in the occurrence rate. The vertical lines indicate the occurrence times of events with magnitude $6 \leq M < 7$ (dotted), $7 \leq M < 8$ (dashed), and $M \geq 8$ (solid). The panel with bold axes, covering the period from March 16 to April 2, 2014, contains the Iquique earthquake. According to the Bayesian inference the q parameter is considered as a random variable and therefore we are also able to estimate its posterior probability distribution at each time window, and obtain its estimate in terms of posterior mean (black dots in Figure 2) as well as a measure of the accuracy of the estimate through the 50% and 90% credible intervals, which span the 25%–75% quantiles and the 5%–95% quantiles, respectively. These intervals are represented by vertical gray and light gray segments in Figure 2.

We summarize the trend of the estimates of the q index evaluated over all time windows, from 2011 to 2024, through their mean (1.565) and first-third quartiles (1.523 - 1.591), indicated by solid and dashed horizontal lines respectively in Figure 2.

Observing Figure 2 we note that:

- the estimate of the q-index is below the first quartile up to the end of July 2013 - we can identify this as a period of background activity;

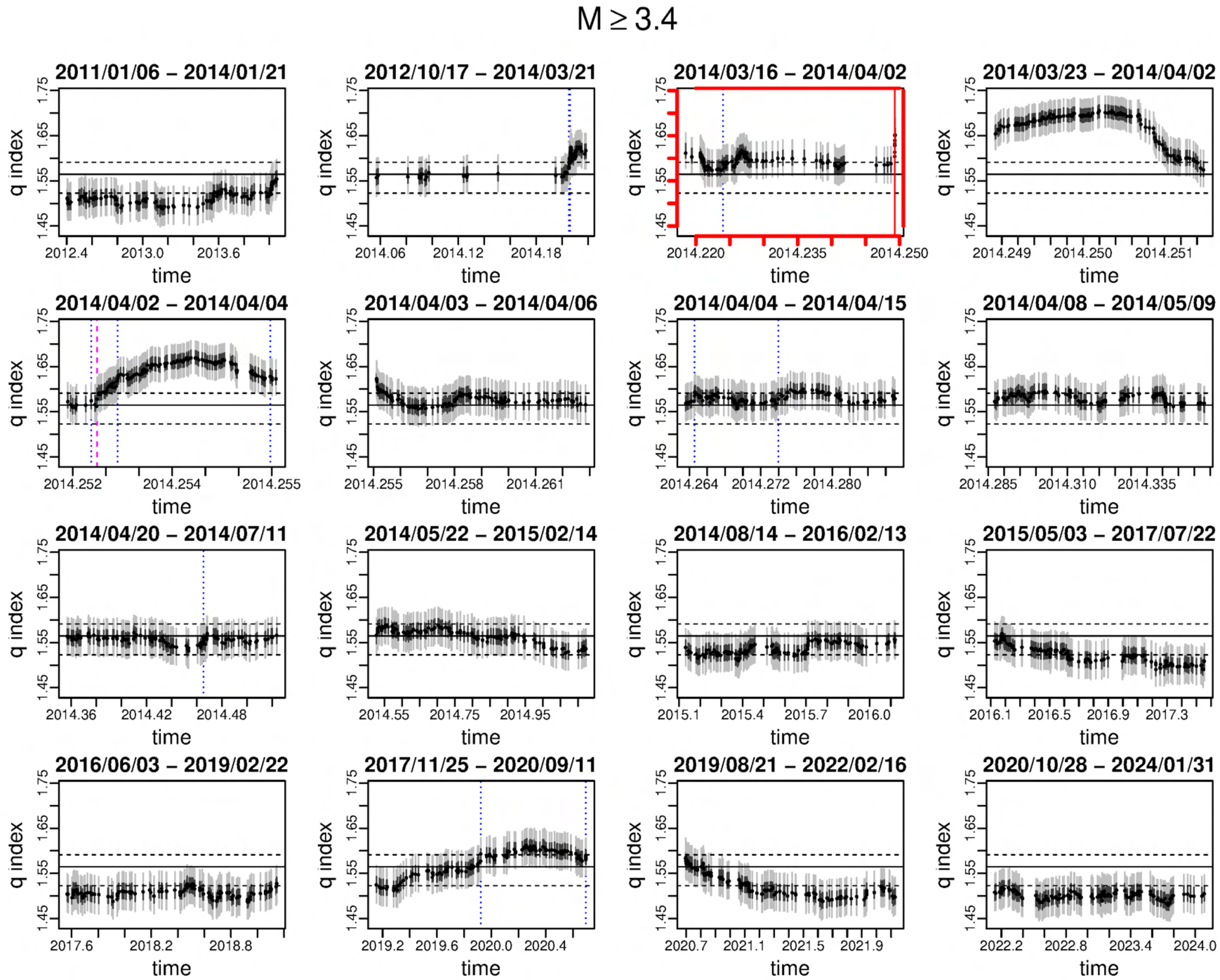

Figure 2: Estimates of the q index for each time window, with the 50% and 90% credible intervals represented by vertical gray and light gray bars, respectively. The mean of the estimated values is represented by the solid horizontal line, while the dashed horizontal lines denote the first and third quartiles. Vertical lines indicate the occurrence times of events with different magnitudes: $6 \leq M < 7$ (dotted), $7 \leq M < 8$ (dashed), and $M \geq 8$ (solid). Time is shown in decimal format.

- then the value of the q-index starts to grow, exceeding the mean around February 2014 and the third quartile in mid-March 2014, just after the first of the three $6 < M < 7$ events - we denote this period as preparatory phase, namely a period in which the estimated magnitude distribution begins to show heavier tail than that estimated in a period of background activity, making strong earthquakes more likely;
- the entropic index reaches the highest values immediately after the Iquique shock (main phase) and its trend is decreasing during the aftershock sequence;
- the same increasing trend, albeit more limited, is also observed during the two shocks with $M = 6$ shocks in 2019-2020 but the reversal of the trend after the second shock suggests that most of the energy has been released.

Figure 3 displays the sequence of the q estimates as a whole and the two lower panels depict enlargements of the main panel (above) around the main shock: on the left there are the values from April to December 2013, and on the right those associated with windows from January 2014 to the main shock; the value of the q-index associated with the window ending at the main shock is indicated by the square. Also, the vertical lines at the bottom in Figure 3 indicate the occurrence times of the events with $6 < M < 7$ (dotted) and $M = 8.2$ (solid), and the horizontal lines correspond to the mean (solid line) and the first and third quartiles (dashed lines) of the estimates. In Figure 3 we note more clearly what we have already emphasized about the significant increase of the value of q during the foreshock activity. Moreover we note that

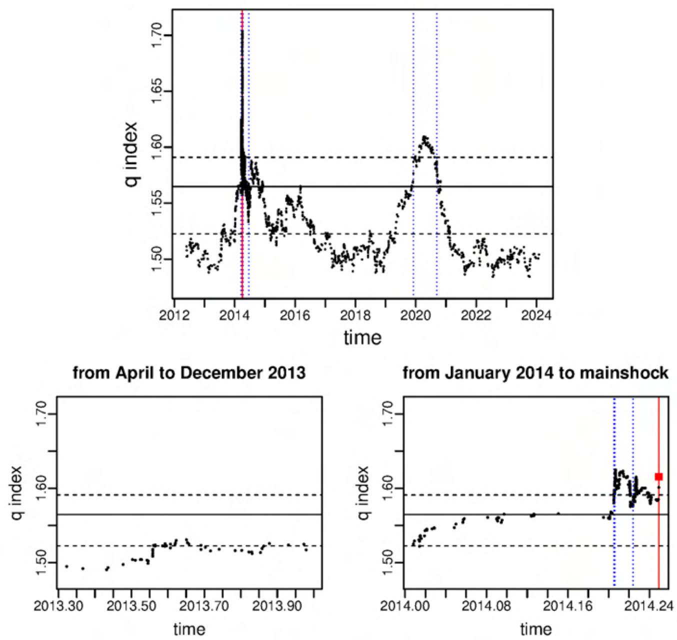

Figure 3: Estimates of the q-index for each shifting window. Bottom: A close-up of the parameter estimates surrounding the Iquique mainshock, with the square highlighting the entropic index value for the window ending at the mainshock.

- the q-index has a globally decreasing phase up to 2018, then it reverses the trend by raising up to the time interval between the two $M = 6$ shocks;
- afterwards a new decreasing phase begins which lasts until the end of 2021, followed by an increasing trend which, however, has not yet reached the interquartile range of the estimates of q that can be associated with a preparatory phase, i.e. a warning period preceding possible strong earthquakes.

It could be hypothesized that when the value of the q-index increases and as long as it remains high (at least in the estimated interquartile range of the region under study), we have to expect further releases of energy. We emphasize that to apply this warning criterion the interquartile range must be calculated on a sufficiently large data set which includes at least a seismic cycle, that is, a period formed by preparatory phase, strong event and aftershock sequence.

For comparison, we also fitted the exponential distribution (3) to the magnitude data within the same sliding time windows. Following the criterion of the maximum posterior marginal log-likelihood, as described in the *Theoretical elements* section, it turns out that the q-exponential distribution outperforms the exponential one in most cases; in particular, the maximum difference $\mathcal{L}_{log}\, f_{(q-exp)}(\mathbf{x})) - \mathcal{L}_{log}\, f_{(exp)}(\mathbf{x})$ is obtained in the time window spanning from 3 April 2014 to 4 April 2014, that is, the first days after the main shock, while the maximum difference $\mathcal{L}_{log}\, f_{(exp)}(\mathbf{x})) - \mathcal{L}_{log}\,(f_{(q-exp)}(\mathbf{x})$ is obtained in the time window located towards the end of the aftershock sequence, from 5 May to 14 June 2014.

Just to visualize how each model fits the data, we use the P-P plot to compare the empirical and theoretical probability distributions (Figure 4). To built the P-P plot, the first step is to sort the magnitude data and obtain the order statistics $M_{(1)} \le M_{(2)} \le \ldots \le M_{(100)}$, which represent the empirical quantiles at which to evaluate the model F; the plotting positions are then $(j/101, F(M_{(j)})$. The more linear the plot, the better the fit to the data. Figure 4 reports the P-P plots related to the two above-mentioned windows, from 3 to 4 April 2014 (top panels) and from 5 May to 14 June 2014 (bottom panels). The left and middle upper panels show the fitting of the plug-in q-exponential and exponential distributions to the magnitude data, respectively, with the histogram of the data displayed in the right panel. The 90% credible intervals are also shown and were evaluated as follows:

- we draw S parameter values $\theta_i, i = 1, \ldots, S$, from the Markov chain generated through the Metropolis-Hasting algorithm (see *Bayesian inference* section) and we sample a set of 100 magnitude values, $\tilde{\mathcal{M}}_i = \{\tilde{M}_{1,i}, \ldots, \tilde{M}_{100,i}\}$, from the corresponding distribution $F(\cdot; \theta_i)$ for each $i = 1, \ldots, S$.
- we order the set $\tilde{\mathcal{M}}_i$ and evaluate the theoretical distribution in it by obtaining $F(\tilde{M}_{(j),i}; \theta_i)$, $j = 1, \ldots, 100$, for each $i = 1, \ldots, S$; fixing j, the set $\{F(\tilde{M}_{(j),1}), \tilde{M}_{(j),2}), \ldots, F(\tilde{M}_{(j),S})\}$ expresses the uncertainty of the model, which is to be compared with the corresponding value $j/101$ of the empirical distribution.
- by ordering and taking the 5% and 95% values of this set, we get the 90% credible interval of $F(\cdot)$ at the j-th order statistic, that is to be compared with $F(M_{(j)}; \hat{\theta})$ of the plug-in distribution at the j-th ordered observation.

For the window from 3 to 4 April 2014 (top panels in Figure 4), 56 and 51 data points out of 100 fall within the 90% credible intervals of the estimated q-exponential and exponential posterior models, respectively. Similarly, for the window from 5 May to 14 June 2014 (bottom panels in Figure 4), there are 99 and 88 data points out of 100 within the 90% credible intervals of the estimated q-exponential and exponential posterior models, respectively. Both models perform better in the second time window (bottom panels) than in the first (top panels), which is consistent with the smoother pattern of the data shown in the histogram.

Analysis of the spatial distribution of epicenters

The spatial location of seismic events can be considered as another descriptor of the seismic activity (Rotondi and Varini, 2022); to investigate the temporal variations of this feature, we consider the same moving time windows of 100 events used in the previous section and we compute

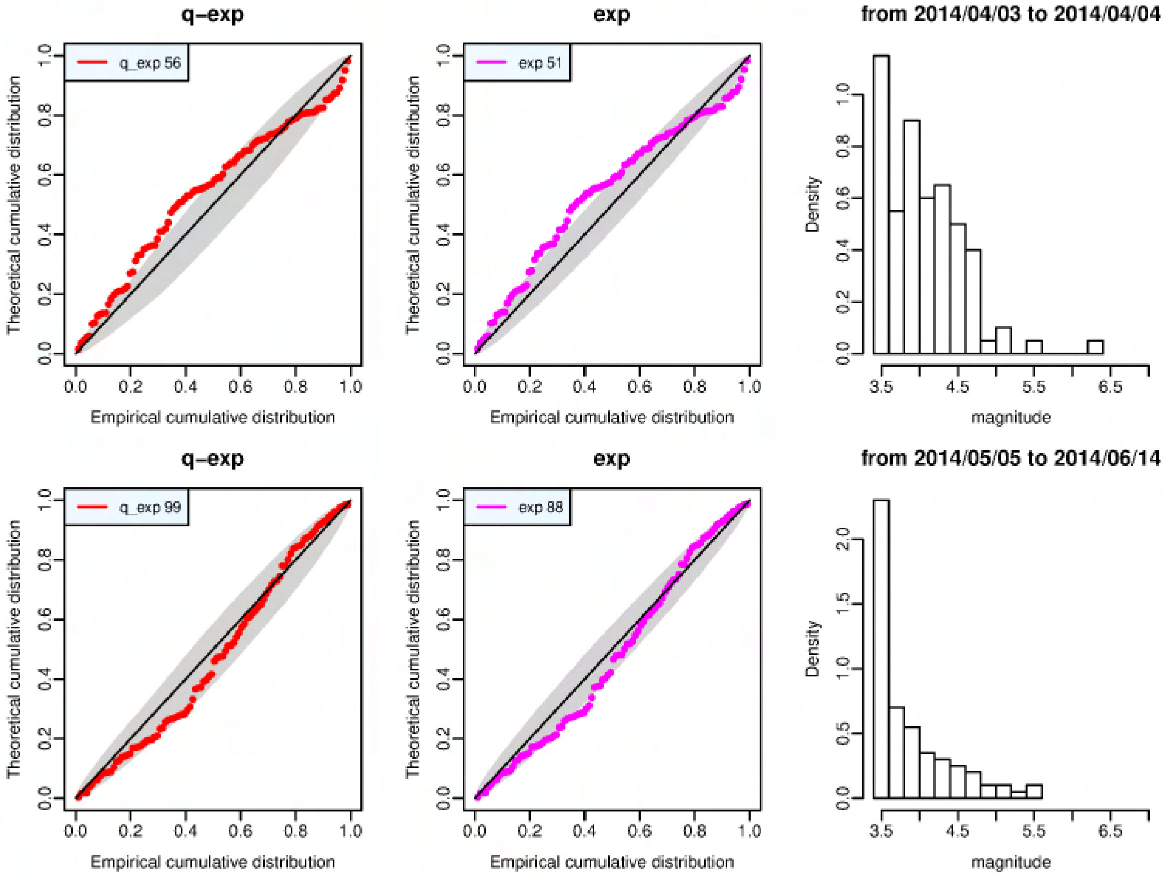

Figure 4: The top (bottom) panels refer to the time window in which the q-exponential (exponential) model outperforms the exponential (q-exponential) model, showing the largest discrepancy in posterior marginal log-likelihood estimates. The right panels display histograms of the magnitude data in these time windows, while the left panels show P-P plots comparing the empirical cumulative distribution with the plug-in q-exponential model (dots), and the middle panels compare it with the exponential model (dots). The straight line represents the ideal fit. All P-P plots include 90% credible intervals (gray band), and the number of data points out of 100 within these intervals is reported in the legend.

the Voronoi tessellations of the Iquique region generated by the epicenters of the earthquakes (seeds) that belong to each window. We construct the Voronoi diagram through the *deldir* package (Turner, 2018), in R programming language (R Core Team, 2018), that uses the Euclidean distance; therefore we convert the latitude and longitude coordinates of the epicenters to planar Universal Transverse Mercator (UTM) coordinate system (in km) by means of the Generic Mapping Tools (GMT) (Wessel and Smith, 1998).

Figure 5 is produced by the 100 earthquakes included in the first time window that covers the period from 2011/01/06 to 2012/05/27; the left picture represents the Voronoi tesselation generated by the epicenters, while the right picture is the Delaunay triangulation of the convex hull of these points (dots).

We propose the four probability distribution functions introduced in the *Theoretical elements* section to model the area of the Voronoi cells: the exponential, the q-exponential,

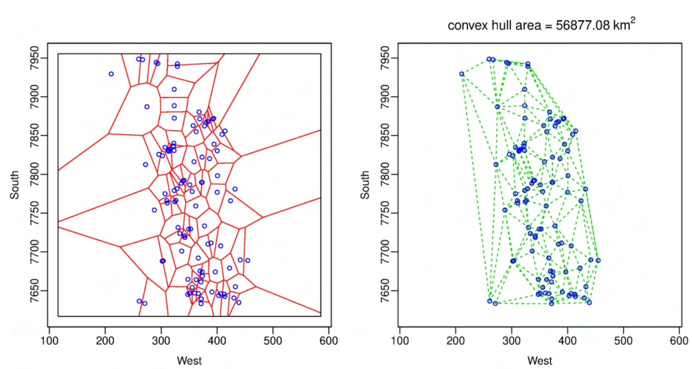

Figure 5: Voronoi tessellation generated by the epicenters (dots) of the events included in the first time window (left) and the convex hull of these points (right); edges of the Voronoi cells (solid lines) and Delaunay triangulation associated with the Voronoi diagram (dashed lines).

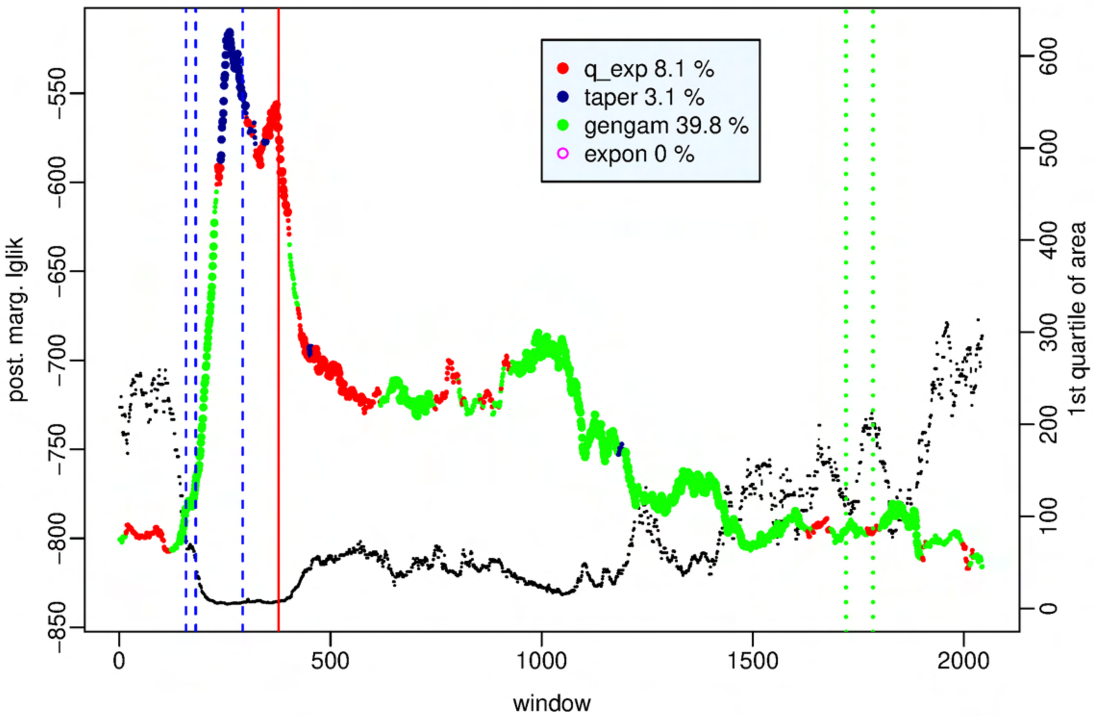

Figure 6: Posterior marginal log-likelihood of the probability distribution for the Voronoi cell area that best fits the dataset for each time window. Vertical lines indicate the windows ending on the day of the mainshock (solid line), the $6 < M < 7$ foreshocks (dashed lines), and the $M = 6$ events (dotted lines). The small black dots indicate the first quartile of the set of cell areas within each window and the legend provides the percentages of time windows in which each model performs better than the others with strong evidence.

the tapered Pareto, the generalized gamma distributions. Also in this case we follow the Bayesian paradigm and compare the four probability distributions on the basis of their posterior marginal log-likelihoods.

Figure 6 shows the value of the posterior marginal log-likelihood for the best distribution at each window; the strong/weak evidence in favor of this model with respect to the second best model is denoted by the large/small size of the dot. The first quartile of the cell areas in each time window is also represented (small black dots), along with the percentage of time windows in which each model outperforms the others with strong evidence (as indicated in the legend). The same holds in Figure 7 that provides a magnification around the occurrence time of the Iquique earthquake in the months from 2 February to 2 April 2014.

Observing Figures 6 and 7 we note that the first quartile of the cell areas decreases rapidly starting from January 2014 when the convex hull containing the epicenters covers about km^2 60,000, it reaches the minimum - 4.95 - at the window ending on 21 March 2014 with convex hull of km^2 2,480.61 and it remains lower than 40 in the first hours after the mainshock. In other words this means that the seismic activity is increasingly concentrated along the rupture line of the forthcoming strong earthquake since the beginning of 2014 and

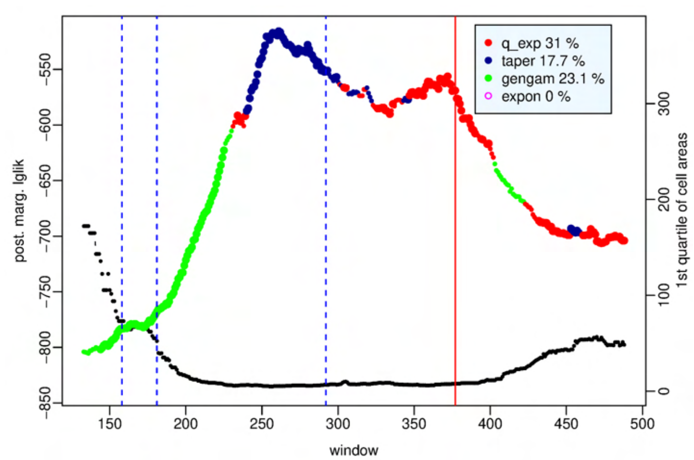

Figure 7: A close-up of Figure 6 focusing on the period from February 2 to April 2, 2014 (hour 18, one day after the Iquique earthquake). As in Figure 6, the small black dots represent the first quartile of the set of cell areas within each time window.

then it begins to slowly spread to greater distances from the fault area. On the contrary, the value of the log-likelihood behaves in opposite way: it noses up in early 2014 and starts to decrease after the mainshock. Note that nothing similar occurs in the period that includes the two events of $M = 6$

between December 2019 and September 2020. Summarizing we can say that:

- the significant increase in the posterior marginal log-likelihood indicates that seismicity begins to concentrate around the possible rupture area of a strong shock (foreshock activity); at the same time the evidence shifts from the generalized gamma model in favor of the tapered Pareto model (preparatory phase);
- the q-exponential distribution, having the heaviest tail, is the optimal model in the period of maximum concentration of the seismicity that includes the main shock occurrence (primary clustering phase), characterized by Voronoi cells with very small areas in the rupture zone and surrounded by a few very large cells (see top-left panel in Figures 9 and 10);
- the generalized gamma distribution characterizes the less active part of the aftershock sequence when the concentration of events spreads over a larger area surrounding the seismogenic area (secondary clustering phase), and later, when the posterior marginal log-likelihood decreases, the same distribution fits the spatial behavior of the background activity better than the other models.

Also in this spatial analysis we performed a sensitivity analysis by varying the number of events considered in each time window between 50 and 200; the results, reported in detail in the Supplemental Material, support those described in this section. In Figures 8, 9, and 10, we examine in detail the time windows in which the three probability distributions: generalized gamma, tapered Pareto, and q-exponential are respectively the best model from the point of view of the posterior marginal log-likelihood, that is, the time windows in which the posterior marginal likelihood of each model has the maximum value and the maximum difference from that of the other two models. The top panels show the Voronoi tessellation (left) and the Delaunay triangulation (right) generated by the epicenters of the 100 events that occurred in that time window; at bottom, we find the histogram of the set of the cell areas in the left-hand panel and the P-P plot of the four distributions, including also the exponential, in the right-hand panel.
The legend in the bottom right panel reports the average absolute difference between theoretical and empirical distributions for each distribution. In temporal order, we first find the window that goes from 10 November 2013 to 17 March 2014 (see Figure 8) where the generalized gamma distribution is the best model, able to better fit a spatially more scattered seismic activity, while the q-exponential distribution provides the best performance in the window from 22 to 29 March 2024 that is closer to the main shock and in which the events are even more concentrated around the Iquique epicenter (see Figure 10). The intermediate position is occupied by the tapered Pareto distribution, the best model in the interval from 24 February to 18 March 2014 (see Figure 9). The P-P plots of the three probability models in the three time windows are presented separately in Figure 11, where the respective credible intervals have been added. The legends report how many data points fall in the credible intervals. We note that, in these windows, the best model in terms of posterior marginal log-likelihood has also the maximum number of data points within its credible interval, as indicated in the darkest legends.

Conclusions

The aim of our work has been to investigate possible correlations between variations in the probability modelling of seismic quantities such as the magnitude and the spatial location of earthquakes, and different phases of a seismic cycle such as the period that precedes a strong shock, or that of background activity, or that characterized by an aftershock sequence. To do that we have considered the seismogenic zone in northern Chile hit by the $M = 8.2$ earthquake of Iquique on 1 April 2014 and we have analyzed the last 13 years of the seismic activity recorded in that region by estimating various probability models on the sequence of magnitude values and on the spatial pattern generated by the epicenters. As regards the magnitude, the increase and the presence of the q-entropic parameter that characterizes the q-exponential distribution chosen as model in an interval of critical values can be a signal of impending energy release. In the case of the spatial distribution of the events we have noted that the probability model that best fits the data changes in the phase preceding the strong earthquake and in the initial part of the aftershock sequence. In this case we can therefore say that there are signals that a new phase is approaching when variations in the probability models are observed.

The same analyses were performed in a seismogenic zone of the Central Italy hit by the L'Aquila $M_w = 6.1$ earthquake on 6 April 2009 (Rotondi et al., 2022); given the different energy release scale, this magnitude value is high for the Italian seismicity and, in fact, the earthquake caused 308 deaths, approximately 1,500 injured, and great economic loss. The analyzed data set consisted of 2, 725 events of magnitude at least 2.0, which occurred from 7 April 2005 to the end of July 2009; similarly to the Iquique earthquake, L'Aquila shock was preceded by a $M_w = 4$ foreshock on 30 March 2009. As regards the magnitude analysis, the results obtained in that case share the main conclusions with the present work; in particular we noted that:

- the q index decreases before an earthquake of middle-to-high magnitude and increases rapidly after it;
- the increase in the q index starts with the foreshock activity, spawning the so-called preparatory phase (De Santis et al., 2011); the return of the value of q within

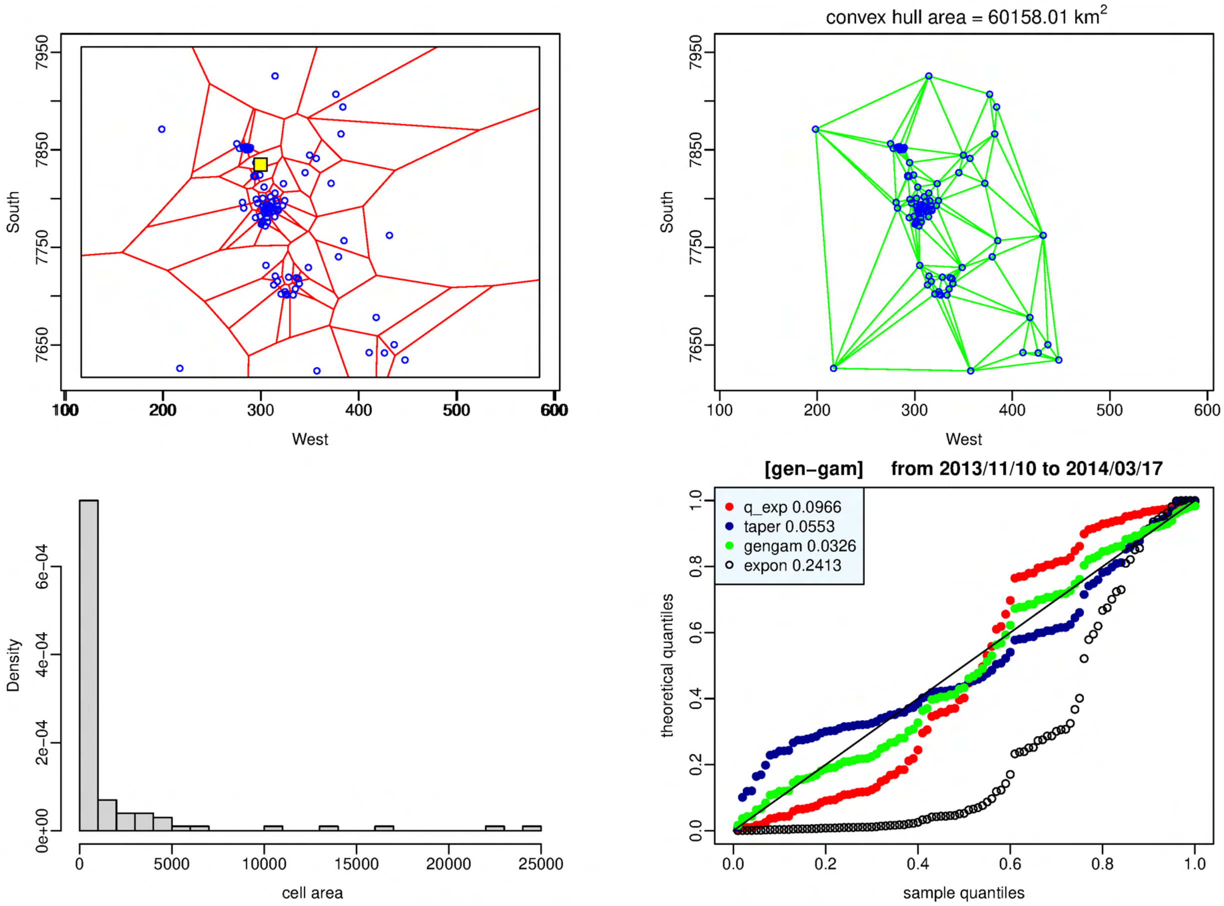

Figure 8: Dataset from the time window where the generalized gamma distribution offers the best fit. Top section: Voronoi tessellation (left) and Delaunay triangulation (right). Bottom: histogram of the cell areas (left) and P-P plot of the four probability distributions (right). The square (top left panel) marks the epicenter of the Iquique shock.

the interquartile range may also indicate the end of the aftershock activity.

- if with seismic crisis we mean the combination of the preparatory, main and recovery phases introduced by De Santis et al. (2011), we can say that the q index shows a significant and persisting decrease before the onset of a seismic crisis, which indicates energy concentration, followed by a sudden increase that corresponds to energy dissipation.

As regards the spatial analysis (Rotondi and Varini, 2022), the comparison with the Italian situation is more complex, perhaps because this analysis is more influenced by the different tectonic mechanism, as well as very different seismicity rate and characteristics of the rupture zone. However, the main conclusions are in agreement; in particular we note that in both cases the q-exponential distribution characterizes the aftershock period, the tapered Pareto distribution the preparatory phase and the generalized gamma distribution the background activity, while the exponential distribution is the best model in a short period preceding the onset of the seismic crisis in the Italian case study but not in the Chilean one.

In conclusion, we analyzed the temporal variations of space-magnitude probability distributions in seismic sequences characterized by a strong earthquake preceded by foreshocks in two very different tectonic environments. The results agree in associating seismic phase changes to the variations of the best probability model and therefore provide useful indications for the implementation of risk mitigation actions. We are aware that a strong earthquake is not always preceded by less violent but significant shocks as instead happened in the cases described; however, we believe that the proposed method is still useful, at least when this happens, to recognize the signals of an incoming seismic crisis. Of course, this approach should be applied in other seismotectonic contexts to strengthen the proposed conclusions.

Data and Resources

All data used in this paper were provided in different period by the National Seismological Center of the University of Chile (https://www.sismologia.cl/) on request of the authors.

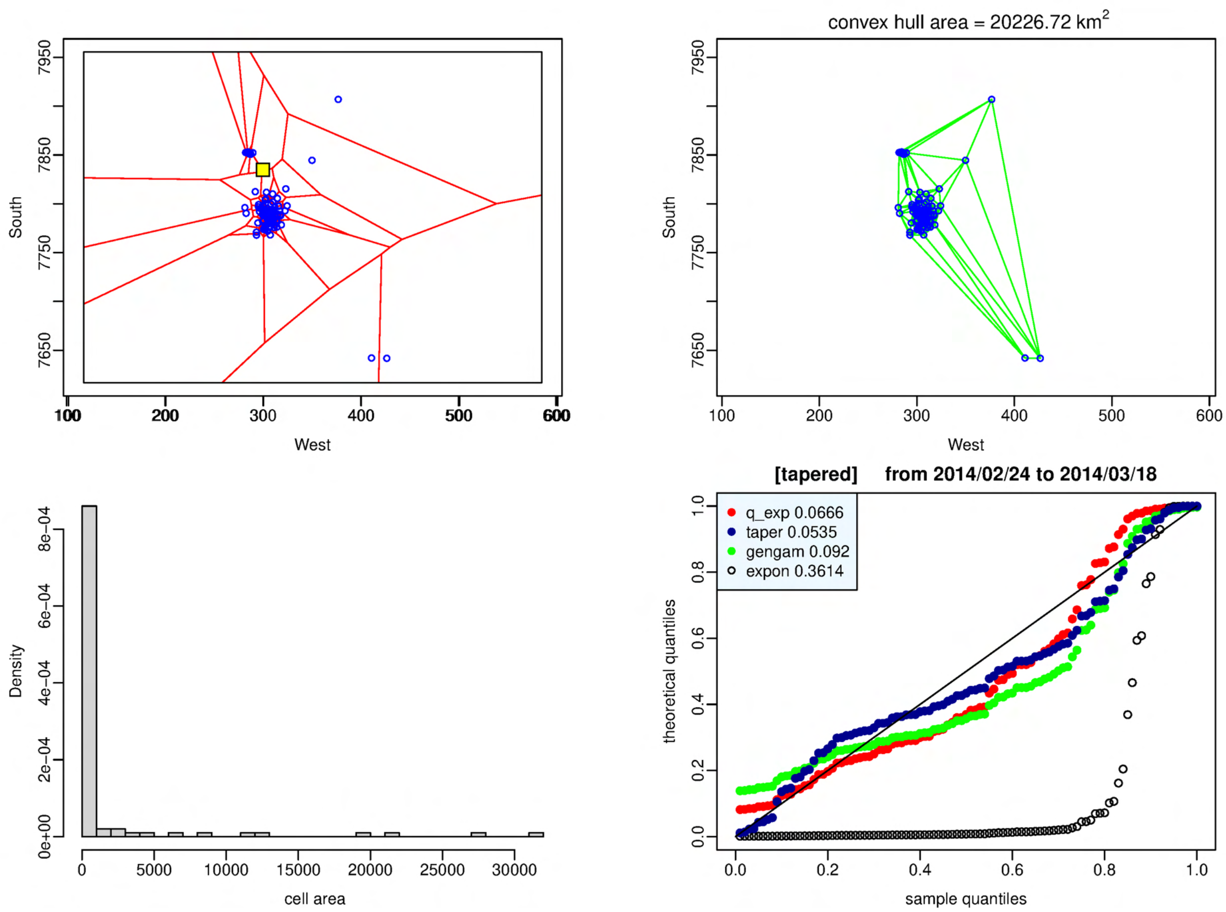

Figure 9: As Figure 8 where the tapered Pareto distribution represents the best fit.

The last data submission was on February 27, 2024. Figure 1 was made using the Generic Mapping Tools version 4.2.1 (www.soest.hawaii.edu/gmt; Wessel and Smith, 1998). A graphical exploratory analysis of the earthquake data and the sensitivity analysis to the choice of the number of events in the moving window method are provided in the *Supplemental Material*.

Declaration of Competing Interests

The authors acknowledge that there are no conflicts of interest recorded.[1]

Acknowledgments

E.V. acknowledges the support of ICSC National Research Centre for High Performance Computing, Big Data and Quantum Computing (CN00000013, CUP B93C22000620006) within the European Union-NextGenerationEU program. Views and opinions expressed are however those of the authors only and do not necessarily reflect those of the European Union or the European Commission. Neither the European Union nor the European Commission can be held responsible for them.

O.N. was partially supported by Chilean National Agency for Research and Development (ANID), Fondecyt grant ID 1241881, and by the Research Center for Integrated Disaster Risk Management (CIGIDEN), ANID/FONDAP/1523A0009.

[1]The authors acknowledge that there are no conflicts of interest recorded.

References

Barrientos, S. and N. S. C. C. Team (2018). The seismic network of Chile. *Seismological Research Letters* **89**(2A), 467–474.

Contreras-Reyes, E., S. Obando-Orrego, J. Geersen, and J. P. Bello-González (2021). Density structure, flexure, and tectonics of the iquique ridge, northern chile. *Journal of South American Earth Sciences* **111**, 103423.

De Santis, A., G. Cianchini, P. Favali, L. Beranzoli, and E. Boschi (2011). The Gutenberg-Richter law and entropy of earthquakes: Two case studies in central Italy. *Bull. Seism. Soc. Am.* **101**(3), 1386–1395.

Gelman, A., J. Carlin, H. Stern, and D. Rubin (2004). *Bayesian Data Analysis*. Chapman & Hall.

Gezer, F., R. Aykroyd, and S. Barber (2021). Statistical properties of Poisson-Voronoi tessellation cells in bounded regions. *J. Statist. Comput. Simul.* **91**(5), 915–933.

Hayes, G. P., M. W. Herman, W. D. Barnhart, K. P. Furlong, S. Riquelme, H. M. Benz, E. Bergman, S. Barrientos, P. S. Earle, and S. Samsonov (2014). Continuing megathrust earthquake potential in Chile after the 2014 Iquique earthquake. *Nature* **512**(7514), 295–298.

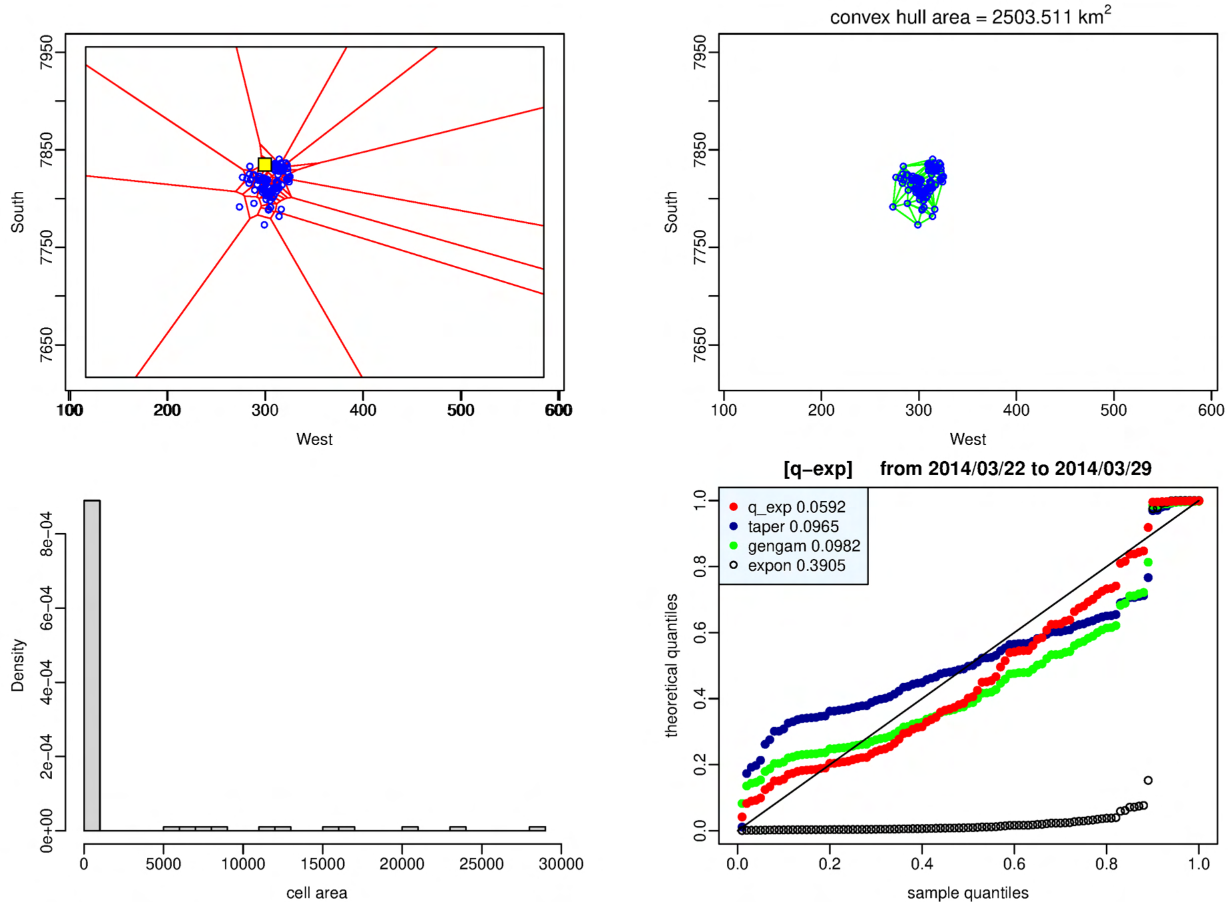

Figure 10: As Figure 8 where the q-exponential distribution represents the best fit.

Jackson, D. and Y. Kagan (1999). Testable earthquake forecasts for 1999. *Seismological Research Letters* **70**(4), 393–403.

Kass, R. and A. Raftery (1995). Bayes factor. *J. Am. Stat. Ass.* **90**(430), 773–795.

Lasocki, S., V. G. Karakostas, F. Ramón Zúñiga, E. E. Papadimitriou, and Y. Mahmood (2024). Premonitory earthquakes clustering process in an equivalent dimensions space before the 2017 M_w 8.2 Tehuantepec, Mexico, mainshock. *Seismol. Res. Lett.*, 1–13.

Ma, B., J. Geersen, D. Klaeschen, E. Contreras-Reyes, M. Riedel, Y. Xia, A. M. Tréhu, D. Lange, and H. Kopp (2023). Impact of the iquique ridge on structure and deformation of the north chilean subduction zone. *Journal of South American Earth Sciences* **124**, 104262.

Meng, L., H. Huang, R. Bürgmann, J. P. Ampuero, and A. Strader (2015). Dual megathrust slip behaviors of the 2014 Iquique earthquake sequence. *Earth and Planetary Science Letters* **411**, 177–187.

Posadas, A., D. Pasten, E. E. Vogel, and G. Saravia (2023). Earthquake hazard characterization by using entropy: Application to northern chilean earthquakes. *Natural Hazards and Earth System Sciences* **2023**, 1–22.

Posadas, A. and O. Sotolongo-Costa (2023). Non-extensive entropy and fragment–asperity interaction model for earthquakes. *Communications in Nonlinear Science and Numerical Simulation* **117**, 106906.

Prentice, R. (1974). A log gamma model and its maximum likelihood estimation. *Biometrika* **61**(3), 539–544.

R Core Team (2018). *R: A Language and Environment for Statistical Computing*. Vienna, Austria: R Foundation for Statistical Computing.

Robert, C. P. and G. Casella (2004). *Markov Chains*, pp. 205–265. New York, NY: Springer New York.

Rotondi, R., G. Bressan, and E. Varini (2022). Analysis of temporal variations of seismicity through non-extensive statistical physics. *Geophys. J. Int.* **230**, 1318–1337.

Rotondi, R. and E. Varini (2022). Temporal variations of the probability distribution of Voronoi cells generated by earthquake epicenters. *Front. Earth Sci.* **10.938348**.

Ruiz, S., M. Metois, A. Fuenzalida, J. Ruiz, F. Leyton, R. Grandin, C. Vigny, R. Madariaga, and J. Campos (2014). Intense foreshocks and a slow slip event preceded the 2014 Iquique M w 8.1 earthquake. *Science* **345**(6201), 1165–1169.

Schoenberg, F. P., C. Barr, and J. Seo (2009). The distribution of Voronoi cells generated by Southern California earthquake epicenters. *Environmetrics* **20**, 159–171.

Schurr, B., G. Asch, S. Hainzl, J. Bedford, A. Hoechner, M. Palo, R. Wang, M. Moreno, M. Bartsch, Y. Zhang, et al. (2014).

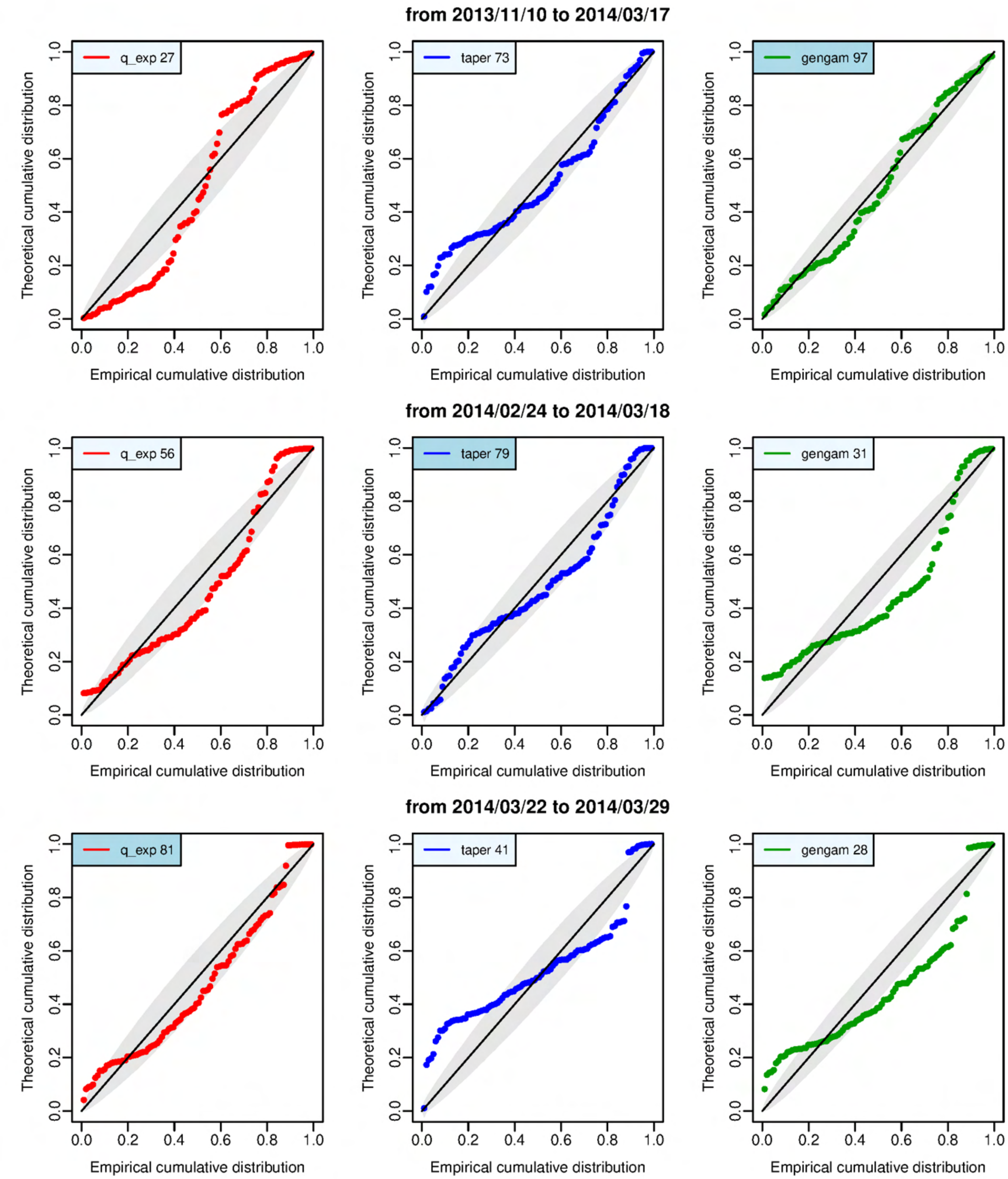

Figure 11: P-P plots comparing the empirical cumulative distribution with the plug-in q-exponential model (dots, left panels), the tapered Pareto model (dots, middle panels), and the generalized gamma model (dots, right panels). The straight line represents the ideal fit. All P-P plots include 90% credible intervals (gray band), and the number of data points out of 100 within these intervals is reported in the legend. Top, middle, and bottom panels refer to the time windows in which the generalized gamma model, the tapered Pareto model, and the q-exponential model perform best, respectively, showing the largest discrepancy in posterior marginal log-likelihood estimates.

Gradual unlocking of plate boundary controlled initiation of the 2014 Iquique earthquake. *Nature* **512**(7514), 299–302.

Sotolongo-Costa, O. and A. Posadas (2004). Fragment-asperity interaction model for earthquakes. *Phys. Rev. Lett.* **92**, 048501.

Stacy, E. (1962). A generalization of the gamma distribution. *Ann. Math. Statist.* **33**, 1187–1192.

Tsallis, C. (1988). Possible generalization of Boltzmann-Gibbs mechanics. *J. Stat. Phys.* **52**, 479–487.

Tsallis, C. (2009). *Introduction to Nonextensive Statistical Mechanics. Approaching a Complex World*. Springer.

Turner, R. (2018). *deldir: Delaunay Triangulation and Dirichlet (Voronoi) Tessellation*. R package version 0.1-15.

Vallianatos, F., G. Papadakis, and G. Michas (2016). Generalized statistical mechanics approaches to earthquakes and tectonics. *Proc. R. Soc. A* **472**, 20160497.

Varini, E. and R. Rotondi (2023). Connection between Variations of the Probability Distribution of the Recurrence Time and Phases of the Seismic Activity. *Entropy* **25**, 1441.

Vere-Jones, D., R. Robinson, and W. Yang (2001). Remarks on the accelerated release model: problems of model formulation simulation and estimation. *Geophys. J. Int.* **144**(3), 517–531.

Wessel, P. and W. Smith (1998). New, improved version of Generic Mapping Tools released. *EOS Trans. Amer. Geophys. U.* **79**(47), 579.

Full mailing address for each author

Renata Rotondi, National Research Council of Italy, Institute for Applied Mathematics and Information Technologies Enrico Magenes, via Bassini 15, 20133 Milano, Italy, email: reni@mi.imati.cnr.it, https://orcid.org/0000-0003-1501-9751

Orietta Nicolis, Universidad Andres Bello, Engineering Faculty, Calle Quillota, 980, Viña del Mar 2520000, Chile, and Research Center for Integrated Disaster Risk Management (CIGIDEN), Av. Libertador Bernardo O'Higgins 340, Santiago 8331150, Region Metropolitana, Chile, email: orietta.nicolis@unab.cl, https://orcid.org/0000-0001-8046-6983,

Elisa Varini, National Research Council of Italy, Institute for Applied Mathematics and Information Technologies Enrico Magenes, via Bassini 15, 20133 Milano, Italy, email: elisa.varini@cnr.it, https://orcid.org/0000-0002-5365-4249

Fabrizio Ruggeri, National Research Council of Italy, Institute for Applied Mathematics and Information Technologies Enrico Magenes, via Bassini 15, 20133 Milano, Italy, email: fabrizio@mi.imati.cnr.it, https://orcid.org/0000-0002-7655-6254

Manuscript Received 00 Month 0000

Supplemental material

Variations of probability distributions as indicators of seismic phases: a case study from Chile

R. Rotondi, O. Nicolis, E. Varini, and F. Ruggeri

Graphical exploratory analysis

The top left panel of Figure S1 shows the magnitude versus sequential number plot of the earthquakes analyzed in the Iquique case study; the vertical lines denote the earthquakes of $6 \le M < 7$ (green), $7 \le M < 8$ (blue), $M \ge 8$ (red). If the dataset is complete, such a plot should show a homogeneous pattern along the horizontal axis; we can see that the most evident missing events are immediately after the strongest shock of Iquique mainly in the range of magnitude $2 \le m_0 \le 3$. The top right panel depicts the magnitude versus time plot; it suggests that the recording level in the catalogue is only acceptable since 2011. These conclusions are confirmed by the bottom panels showing the cumulative number of the events (on left) and the histogram of the magnitude (on right) respectively.

Hence, observing Figure S1, we conclude that:

- the data set is clearly incomplete before 2011 and events of $M < 2.5$ are missing in the recent years between 2016 - 2024 (see top right panel);
- the completeness magnitude could be around $M = 3$ (see bottom right panel);
- partial incompleteness can be observed immediately after the $M = 8.2$ Iquique main shock, due to the difficulty in recording all the events at the beginning of the aftershock sequence. This causes the completeness magnitude to rise up to 3.3 - 3.4 (see top left panel);
- the temporal distribution of the magnitudes is odd: $M6+$ events are rare after 2014, and $M7+$ events are only aftershocks.

Sensitivity analysis

The choice of $m = 100$ as the number of events examined in each window was made to ensure both the accuracy of the parameter estimates and the detail in the analyses; however, we performed a sensitivity analysis of the results by varying this value between 50 and 200. Figure S2 shows the estimates of the q-index obtained using time windows with 50, 100 and 200 events. We can say that the variations are more evident with $m = 50$, while the trend becomes smoother by increasing the value of m; it is still possible to conclude that the global trend remains the same.

As regards the spatial analysis, the left panels of Figure S3 highlight the posterior marginal log-likelihood of the best model among the four considered for the area of the Voronoi cells when using 50, 100, and 200 events as seeds in the generation of the cells; the legends report the percentages of windows in which each model shows strong evidence of being the best model. In the right panels there are close-ups of the same pictures around the occurrence time of the mainshock. The general trend is the same, although it is smoother when m is larger. Looking at the values in the legends we note that with $m = 200$ the q-exponential distribution is the best prevailing model at the expense of the generalized gamma distribution. The common conclusion is that the q-exponential model is associated with a higher concentration of the events and the generalized gamma model with a more sparse activity.

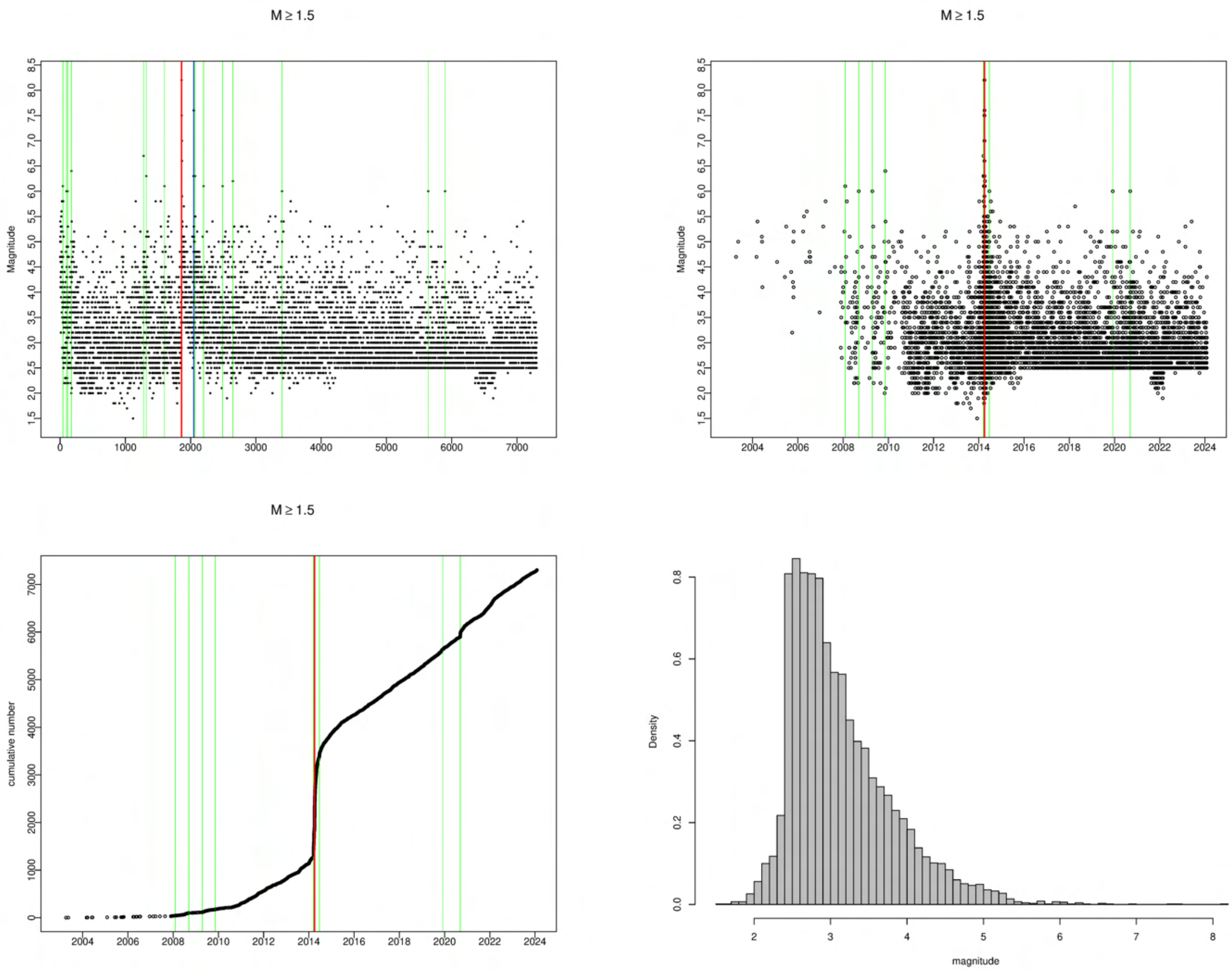

Figure S1: $M \geq 1.5$ - Top left: Magnitude vs event position number; Top right: Magnitude vs time; Bottom left: Cumulative number of events vs time; Bottom right: histogram of the magnitude for bin size of 0.1 degrees. Vertical lines denote the earthquakes of $6 \leq M < 7$ (green), $7 \leq M < 8$ (blue), $M \geq 8$ (red).

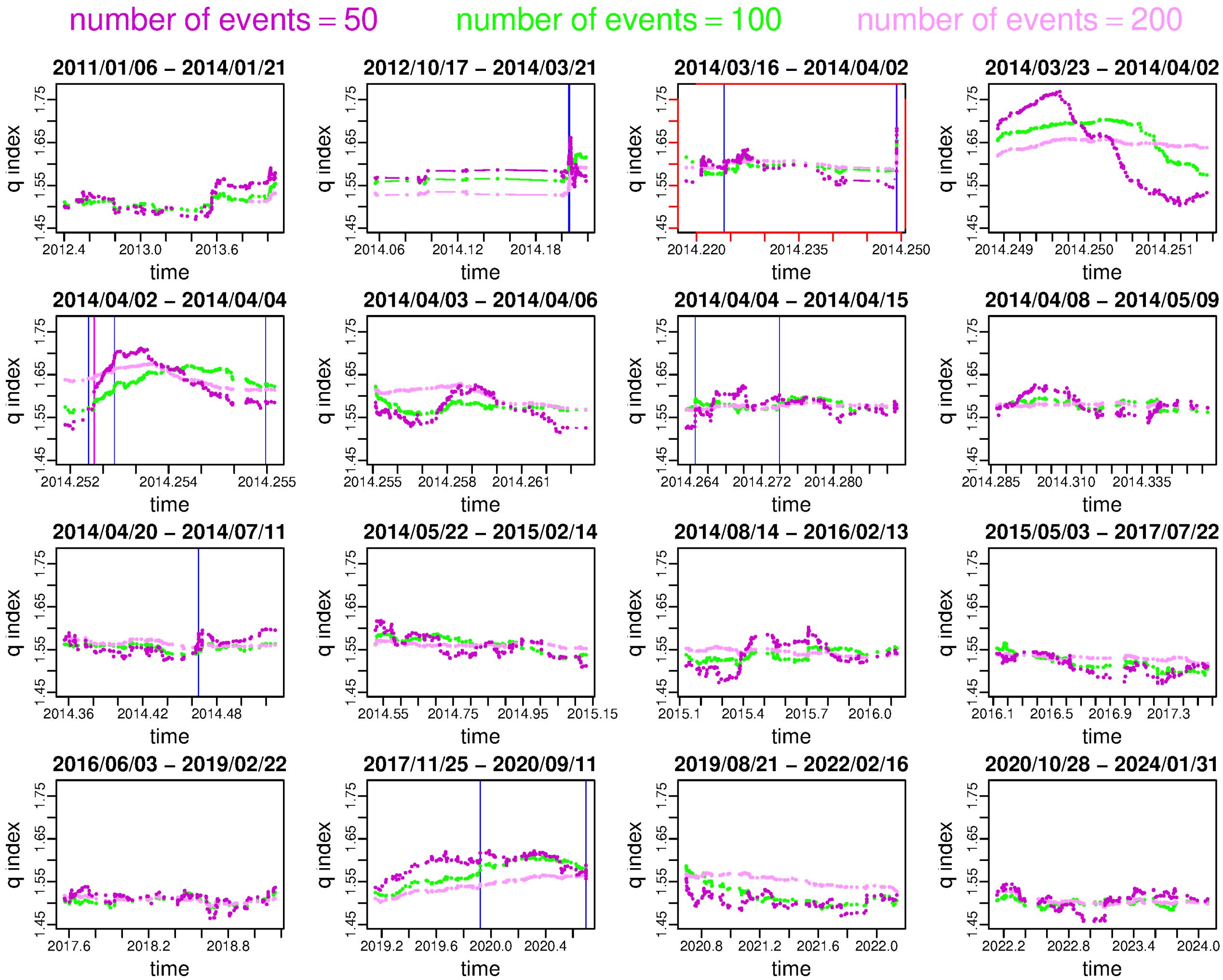

Figure S2: Estimates of the q index at time windows with different number of events. Vertical lines indicate the occurrence times of events with different magnitudes: $6 \leq q < 7$ (blue), $7 \leq q < 8$ (magenta), and $q \geq 8$ (red). The red panel contains the Iquique earthquake.

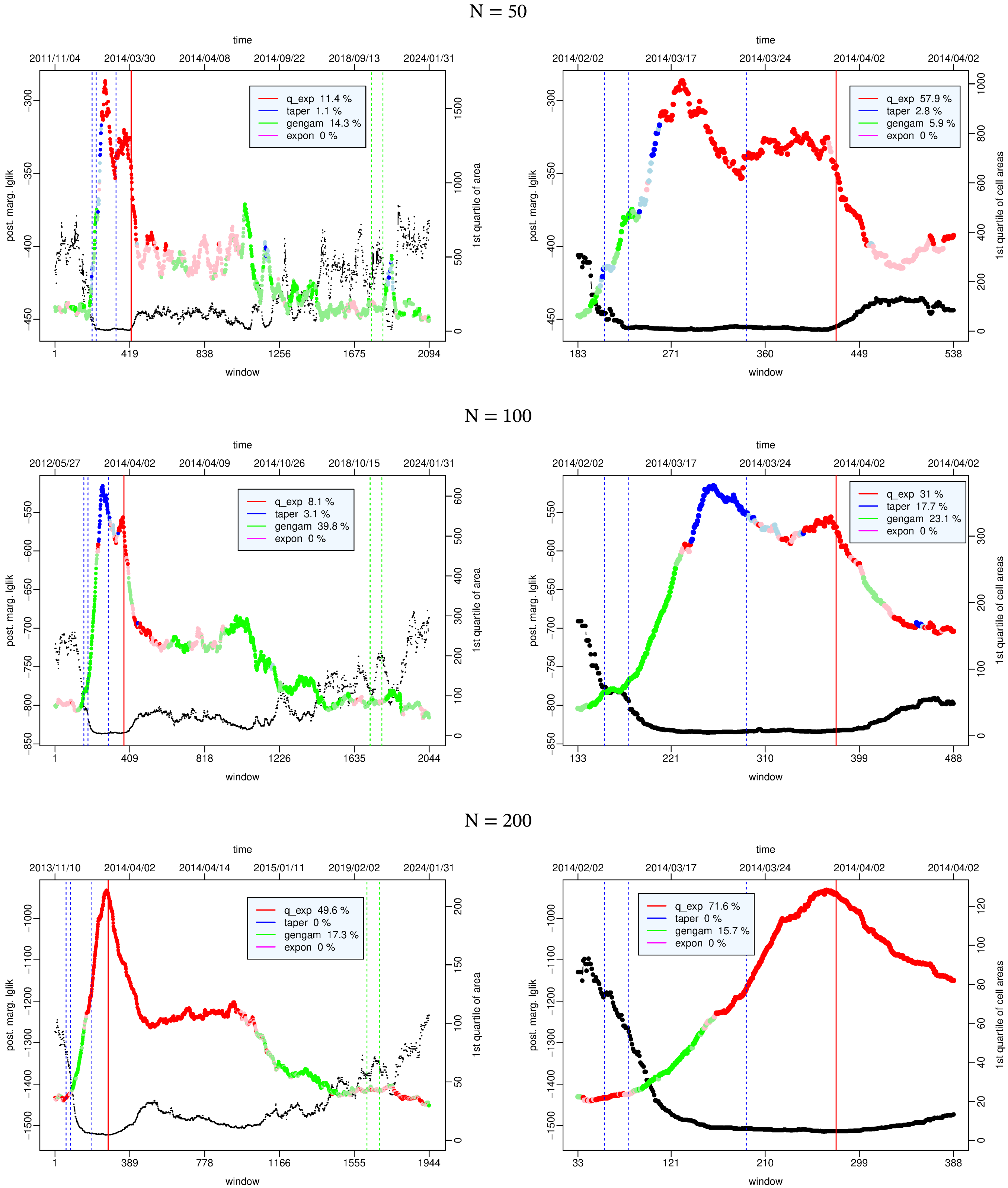

Figure S3: Values of the posterior marginal log-likelihoods for different number of events N in each time window. On right: zoom on the window ending on the Iquique earthquake denoted by the red vertical line. Vertical lines indicate the windows ending on the day of the mainshock (red solid line), the M 6+ foreshocks (blue dashed lines), and the $M = 6$ events (green dashed lines). The legends report the percentages of windows in which each model shows strong evidence of being the best model.